Journal of
Marine Science and Engineering

Article

A Parametric Study on the Interconnector of Solid Oxide Electrolysis Cells for Co-Electrolysis of Water and Carbon Dioxide

Shian Li, Zhi Yang, Qiuwan Shen * and Guogang Yang

Marine Engineering College, Dalian Maritime University, Dalian 116026, China; lishian@dlmu.edu.cn (S.L.); yzhi@dlmu.edu.cn (Z.Y.); yanggg@dlmu.edu.cn (G.Y.)
* Correspondence: shenqiuwan@dlmu.edu.cn

Abstract: The shipping industry is trying to use new types of fuels to meet strict pollutant emission regulations and carbon emission reduction targets. Hydrogen is one of the options for alternative fuels used in marine applications. Solid oxide electrolysis cell (SOEC) technology can be used for hydrogen production. When water and carbon dioxide are provided to SOECs, hydrogen and carbon monoxide are produced. The interconnector of SOECs plays a vital role in cell performance. In this study, a 3D mathematical model of cathode-supported planar SOECs is developed to investigate the effect of interconnector rib width on the co-electrolysis of water and carbon dioxide in the cell. The model validation is carried out by comparing the numerical results with experimental data in terms of a polarization curve. The rib width is varied from 0.2 mm to 0.8 mm with an interval of 0.1 mm. It is found that the cell voltage is decreased and then increased as the rib width increases. When the current density is 1 A/cm^2, the voltages of SOECs with rib widths of 0.2 mm, 0.6 mm, and 0.8 mm are 1.272 V, 1.213 V, and 1.221 V, respectively. This demonstrates that the best performance is provided by the SOEC with a rib width of 0.6 mm. In addition, the local transport processes of SOECs with different rib widths are presented and compared in detail. This study can provide guidelines for the design of interconnectors of SOECs.

Keywords: hydrogen; marine applications; solid oxide electrolysis cells; numerical modeling; interconnector design

Citation: Li, S.; Yang, Z.; Shen, Q.; Yang, G. A Parametric Study on the Interconnector of Solid Oxide Electrolysis Cells for Co-Electrolysis of Water and Carbon Dioxide. *J. Mar. Sci. Eng.* **2023**, *11*, 1066. https://doi.org/10.3390/jmse11051066

Academic Editors: Tatjana Paulauskiene, Jochen Uebe and Ludmila Filina-Dawidowicz

Received: 27 April 2023
Revised: 15 May 2023
Accepted: 16 May 2023
Published: 17 May 2023

1. Introduction

The widespread utilization of fossil fuels has resulted in considerable environmental pollution. Meanwhile, carbon emissions have a significant impact on the global climate [1]. Nowadays, the main energy source for the shipping industry is still fossil fuels. The fourth International Maritime Organization (IMO) greenhouse gas study pointed out that in 2018, the total annual carbon dioxide emissions from global shipping exceeded 1 billion tons, accounting for approximately 2.89% of the world's total emissions. The IMO has set a goal of reducing the carbon intensity of ships by at least 40% by 2030 and reducing greenhouse gas emissions from ships by more than 50% by 2050 compared to 2008 [2]. In order to solve energy and environmental issues, it is essential to use renewable alternatives to fossil energy and carbon-neutral energy technologies [3,4].

The shipping industry is trying to use new types of marine power systems with low/zero emissions. Fuel cells are one of the possible alternative technologies [5]. Fuel cells have advantages such as zero pollution, low noise, and high energy density. Hydrogen is used as the fuel when the fuel cell system is adopted. Hydrogen is a clean and zero carbon fuel. One of the practical and effective paths for the shipping industry to achieve low carbon or even zero carbon emissions targets is to adopt fuel-cell powered ships [6]. Among various hydrogen production methods, the electrolysis of water is currently considered the most feasible and promising technology for large-scale, renewable energy-based hydrogen production [7]. This process of generating green hydrogen from renewable energy electricity is clean and pollution-free, because the production process is decoupled from fossil fuels. The widespread application of green hydrogen in the shipbuilding industry will help reduce ship carbon emissions [8]. Solid oxide electrolysis cells (SOECs) have gained significant attention due to their high efficiency, flexible reactant selectivity, and noble metal-free catalysts. The high operating temperature of SOECs offers thermodynamic advantages and low overpotential losses compared to low temperature electrolysis techniques [9].

SOECs convert electrical energy into chemical energy stored in the syngas produced by the co-electrolysis of water and carbon dioxide. Numerical simulations were performed to investigate the cell performance and transport phenomena of SOECs. Ni et al. [10,11] used a two-dimensional model to examine the effects of feed gas composition and operating temperature on SOEC performance. A two-dimensional tubular SOEC model was developed and then adopted to obtain the optimal operating condition [12]. In addition, the effects of flow arrangement on temperature distribution, ionic current density distribution, conversion rate, and efficiency were investigated and compared in detail. Xie et al. [13] studied the effects of operating temperature, voltage, and species component on SOEC performance. The effect of operating pressure on cell performance was studied by Du et al. [14]. It was reported that the operating voltage increases and then decreases with increasing operating pressure. Kazemour et al. [15] studied the effects of operating temperature, inlet gas composition, and flow mode on the performance of SOEC under water electrolysis and co-electrolysis modes, respectively. The effects of electrode thickness, support type, porosity, and pore size on the performance of SOECs were comprehensively investigated [16]. Menon et al. [17] studied the effects of operating temperature, inlet gas velocity, electrode thickness, and micro-structural properties on the performance of SOECs. Li et al. [18] studied the effect of cathode electrode thickness on the electrochemical reaction of SOECs. The above-mentioned studies mainly focus on the operating conditions and electrode structure parameters of SOECs.

The interconnector is one of the vital components of SOECs. Its flow field design has a significant effect on the performance of SOECs. SOECs with different flow fields were designed and compared in detail [19]. The porous flow field was able to achieve the best performance. Similarly, the performance of SOECs with a metal foam flow field was also studied by Zhao et al. [20]. The results indicate that the utilization of metal foam as a gas flow field can enhance the performance of SOECs. However, SOECs with parallel flow fields are still widely used. There are many studies on the interconnector of solid oxide fuel cells (SOFCs), but the related studies on SOECs are still very few. The impact of the rib on the concentration polarization of anode-supported fuel cells was extensively investigated by Lin et al. [21]. They provided a practical guide for the optimization of interconnector structure. The effects of rib width, pitch width, and contact area resistance between the electrode and the interconnector on cell performance were systematically studied by Jeon et al. [22]. The rib width of fuel cells was also optimized by Kong et al. [23] and Liu et al. [24] to improve cell performance.

The above-mentioned studies mainly focused on the transport processes and performance of SOECs with constant rib and channel widths. The rib and channel widths of interconnectors can significantly affect the gas transport process in the porous electrode and the performance of SOECs. Therefore, it is necessary to reveal the effect of the interconnector of SOECs on local transport phenomena and overall cell performance. A parametric study on the interconnector of SOECs for the co-electrolysis of water and carbon dioxide needs to be carried out.

In this study, a three-dimensional model for the co-electrolysis of water and carbon dioxide in SOECs was developed to study the effect of interconnector rib width on performance and transport phenomena. The gas transport, heat transfer, mass transfer, ion transport, electron transport, and electrochemical and chemical reaction processes within the cell were considered in detail. The mathematical model was verified by comparing the predicted results with experimental results under the same operating conditions. The effects of interconnector rib width on cell performance, chemical reaction rates, velocity, pressure drop, species, and temperature distributions were also presented and analyzed. This study can provide guidelines for the design of interconnectors of SOECs.

2. Model Description

2.1. Computational Domain and Assumptions

A single channel was chosen as the computational domain, as depicted in Figure 1. It consists of several components including the anode interconnector, cathode interconnector, anode flow channel, cathode flow channel, anode active layer (AAL), cathode active layer (CAL), cathode support layer (CSL), and electrolyte layer. The corresponding geometric parameters are summarized in Table 1. The co-flow arrangement is used in the present work. Water and carbon dioxide are supplied into the cathode flow channel and air is provided for the anode flow channel. When electricity is consumed, hydrogen and carbon monoxide are produced. As shown in Figure 1, the x-axis is the direction of gas flow, the y-axis is the direction of cell width, and the z-axis is the direction of cell thickness.

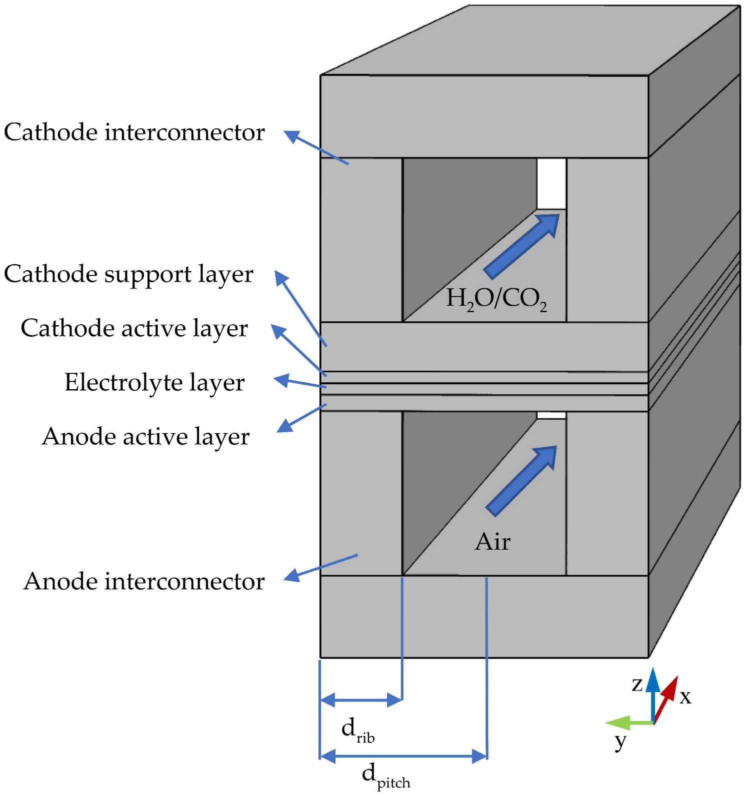

Figure 1. Computational domain of this study.

Table 1. Model geometric parameters.

Parameters	Value
Cell length (L_{cell}, mm)	40
Cell width (W_{cell}, mm)	2
Channel height ($H_{channel}$, mm)	1
Interconnector width (W_{ic}, mm)	2
Interconnector height (H_{ic}, mm)	1.5
Porous electrode length (L_{porous}, mm)	40
Porous electrode width (W_{porous}, mm)	2
CSL thickness (δ_{CSL}, µm)	300
AAL thickness (δ_{AAL}, µm)	15
CAL thickness (δ_{CAL}, µm)	10
Electrolyte thickness (δ_{EL}, µm)	10

The following assumptions were made in this study:

(1) All gases were assumed to be ideal;
(2) The flow was assumed to be incompressible and laminar;
(3) The electrochemical reactions occur in the active layers;
(4) The interconnector material was assumed to be impermeable;
(5) Radiation heat transfer was neglected.

2.2. Governing Equations

Mass, momentum, species, energy, and charge transport equations are included in this mathematical model. The charge conservation equation is:

$$\nabla\cdot\left(-\sigma_i^{eff}\nabla\Phi_i\right)=S_{ion} \tag{1}$$

$$\nabla\cdot\left(-\sigma_e^{eff}\nabla\Phi_e\right)=S_{ele} \tag{2}$$

where σ_i and σ_e are the ionic and electronic conductivities and Φ_i and Φ_e are the ionic and electronic potentials. S_{ele} and S_{ion} are the corresponding source terms, which can be obtained by using the Butler–Volmer equations [25]:

$$i_c=\left(i_{0,c,H_2O}+i_{0,c,CO_2}\right)S_{act,c}\left(\exp\left(\alpha\frac{n_eF\eta}{RT}\right)-\exp\left(-(1-\alpha)\frac{n_eF\eta}{RT}\right)\right) \tag{3}$$

$$i_a=i_{0,a}S_{act,a}\left(\exp\left(\beta\frac{n_eF\eta}{RT}\right)-\exp\left(-(1-\beta)\frac{n_eF\eta}{RT}\right)\right) \tag{4}$$

where α and β are charge transfer coefficients, and η is the activation overpotential. $S_{act,c}$ and $S_{act,a}$ are the anode/cathode effective reaction specific surface area. $i_{0,c,H2O}$ and $i_{0,c,CO2}$ are the exchange current densities for the electrolysis of water and carbon dioxide, and $i_{0,a}$ is the anode exchange current density, which can be calculated from the following equations [14,26]:

$$i_{0,c,H_2O}=\frac{\gamma_{c,H_2O}RT}{2F}\left(\frac{p_{H_2O}}{p_{ref,H_2O}}\right)^m\exp\left(-\frac{E_{act,c}}{RT}\right) \tag{5}$$

$$i_{0,c,CO_2}=\frac{\gamma_{c,CO_2}RT}{2F}\left(\frac{p_{CO_2}}{p_{ref,CO_2}}\right)^m\exp\left(-\frac{E_{act,c}}{RT}\right) \tag{6}$$

$$i_{0,a}=\frac{\gamma_aRT}{4F}\left(\frac{p_{O_2}}{p_{ref,O_2}}\right)^n\exp\left(-\frac{E_{act,a}}{RT}\right) \tag{7}$$

where γ_c and γ_a are adjustable parameters. Experimental work by Li [27] showed that H_2O electrolysis is approximately 2.2 times stronger than CO_2 electrolysis, which was also verified in the SOEC co-electrolysis model by Luo [12], so it is assumed that $\gamma_{c,H2O}$ = $2.2\gamma_{c,CO2}$. E_{act} is the activation energy. In addition, the effective electron and ion conductivities σ_s^{eff} and σ_l^{eff} in the charge conservation equation, which are related to the structural parameters of the porous electrode, including volume fraction and tortuosity, are calculated by the following equations [28]:

$$\sigma_{e,a,LSM}^{eff}=\sigma_{e,a}\frac{V_{LSM,a}}{\tau_{LSM,a}} \tag{8}$$

$$\sigma_{e,c,Ni}^{eff}=\sigma_{e,c}\frac{V_{Ni,c}}{\tau_{Ni,c}} \tag{9}$$

$$\sigma_{i,el,YSZ}^{eff}=\sigma_{i,el}\frac{V_{YSZ,el}}{\tau_{YSZ,el}} \tag{10}$$

where τ is the tortuosity and V is the volume fraction. The superscript denotes the effective and the subscript represents the anode/cathode. The electrodes of the electrolysis cell are composites of an ionic conducting phase (YSZ) and an electronic conducting one (Ni in the cathode and LSM in the anode) [29,30].

$$\sigma_{s,a} = \frac{4.2 \times 10^7}{T} \cdot \exp\left(\frac{-1150}{T}\right) \tag{11}$$

$$\sigma_{s,c} = 3.27 \times 10^6 - 1065.3T \tag{12}$$

$$\sigma_{l,el} = 3.34 \times 10^4 \cdot \exp\left(\frac{-10,300}{T}\right) \tag{13}$$

$$\sigma_{s,ic} = \frac{9.3 \times 10^6}{T} \cdot \exp\left(\frac{-1100}{T}\right) \tag{14}$$

During SOEC operation, the required potential applied to the SOEC can be expressed as [31]:

$$V = E + \eta_{act,c} + \eta_{act,a} + \eta_{ohm} \tag{15}$$

where E is the thermodynamically relevant equilibrium potential (Nernst potential). η_{act} is the activation overpotential reflecting the electrochemical activity of the electrode. η_{ohm} is the ohmic overpotential influenced by ionic and electronic conduction.

The equilibrium potential (Nernst potential) is calculated as follows:

$$E = \frac{1}{x_{H_2O} + x_{CO_2}}\left(x_{H_2O} E_{H_2}^{eq} + x_{CO_2} E_{CO}^{eq}\right) \tag{16}$$

$$E_{H_2}^{eq} = E_{H_2}^0 + \frac{RT}{n_e F} \ln\left(\frac{P_{H_2} P_{O_2}^{0.5}}{P_{H_2O}}\right) \tag{17}$$

$$E_{CO}^{eq} = E_{CO}^0 + \frac{RT}{n_e F} \ln\left(\frac{P_{CO} P_{O_2}^{0.5}}{P_{CO_2}}\right) \tag{18}$$

$$E_{H_2}^0 = 1.253 - 2.4516 \times 10^{-4} T \tag{19}$$

$$E_{CO}^0 = 1.46713 - 4.527 \times 10^{-4} T \tag{20}$$

where E^0 is the temperature-dependent Nernst potential at standard pressure. P_i is the corresponding component partial pressure in atm at the three-phase boundary (TPB). It should be noted that the equilibrium potential includes the concentration overpotential because the partial pressure of the gas at the reaction site is used in the calculations [32].

In porous cathodes, Ni can act not only as an electron conductor but also as a catalyst for the occurrence of water–gas shift reaction (WGSR) and methane steam reforming reaction (MSR) during the co-electrolysis of H_2O and CO_2. The WGSR rate (R_{WGSR}) and MSR rate (R_{MSR}) can be determined by the following widely used expressions of the Habermann model [33]:

$$R_{WGSR} = k_f^{WGSR}\left(p_{H_2} p_{CO} - \frac{p_{H_2} p_{CO_2}}{K_P^{WGSR}}\right) \tag{21}$$

$$R_{MSR} = k_f^{MSR}\left(p_{CH_4} p_{H_2O} - \frac{p_{CO}\left(p_{H_2}\right)^3}{K_P^{MSR}}\right) \tag{22}$$

$$k_f^{WGSR} = 0.0171\exp\left(\frac{-103,191}{RT}\right) \tag{23}$$

$$K_p^{WGSR} = \exp\left(-0.2935Z^3 + 0.6351Z^2 + 4.1788Z + 0.3169\right) \tag{24}$$

$$Z = \frac{1000}{T} - 1 \tag{25}$$

$$k_f^{MSR} = 2395\exp\left(\frac{-231,266}{RT}\right) \tag{26}$$

$$K_p^{MSR} = 1.0267 \times 10^{10} \times \exp\left(-0.2513Z^4 + 0.3665Z^3 + 0.5810Z^2 - 27.134Z + 3.277\right) \tag{27}$$

where k_f is the forward rate constant and K_p is the equilibrium constant, both of which are correlation functions of temperature.

The heat generated/consumed by a chemical reaction can be calculated from the heat of the reaction [34]:

$$H_{MSR} = -(206,205.5 + 19.5175T) \tag{28}$$

$$H_{WGSR} = 45,063 - 10.28T \tag{29}$$

Mass equation:

$$\nabla \cdot (\rho u) = S_{mass} \tag{30}$$

where S_{mass} is the source term of mass equation.

Momentum equation:

$$(u \cdot \nabla)u = \nabla \cdot \left[-pI + \mu\left(\nabla u + (\nabla u)^T\right)\right] + S_{mom} \tag{31}$$

where u is the velocity vector, p is pressure, μ is the dynamic viscosity, and I is the identity matrix.

Momentum conservation with Darcy's term:

$$\frac{\rho}{\varepsilon}\left((u \cdot \nabla)\frac{u}{\varepsilon}\right) = \nabla \cdot \left[-pI + \frac{\mu}{\varepsilon}\left(\nabla u + \nabla u^T\right) - \frac{2}{3}\frac{\mu}{\varepsilon}(\nabla \cdot u)I\right] + S_{mom} \tag{32}$$

where ρ is density, ε is porosity, and S_{mom} is the source term of momentum equation.

Species equation:

$$\nabla \cdot (\rho\omega_i u) + \nabla \cdot (-\rho D_{i,eff} \nabla \omega_i) = S_i \tag{33}$$

where ω is the mass fraction and S_i is the source term of species equation. The effective diffusivity $D_{i,eff}$ can be expressed as [35,36]:

$$D_{i,eff} = \begin{cases} \frac{\varepsilon}{\tau}\left(\frac{1}{D_{i,k} + D_{i,m}}\right)^{-1} & \text{porous electrodes} \\ D_{i,m} & \text{channels} \end{cases} \tag{34}$$

The diffusion coefficient $D_{i,m}$ and the Knudsen diffusion coefficient $D_{i,k}$ can be calculated by using the following equation [37,38]:

$$D_{i,m} = \frac{1 - x_i}{\sum_{j=1, j \neq i}^{n}\left(\frac{x_j}{D_{ij}}\right)} \tag{35}$$

$$D_{i,k} = \frac{2}{3} r_p \sqrt{\frac{8RT}{\pi M_i}} \tag{36}$$

where x is the mole fraction, M is the molar mass, and r_p is the average pore radius. The binary diffusion coefficient can be calculated as [39]:

$$D_{ij} = \frac{0.00101T^{1.75}\left(\frac{1}{M_i} + \frac{1}{M_j}\right)^{\frac{1}{2}}}{p\left(V_i^{\frac{1}{3}} + V_j^{\frac{1}{3}}\right)^2} \quad (37)$$

where V is the diffusion volume.

Energy equation:

$$\rho C_p u \cdot \nabla T + \nabla \cdot (-\lambda_{eff} \nabla T) = S_T \quad (38)$$

where C_p is the specific heat capacity, λ_{eff} is the effective thermal conductivity, and S_T is the source term of energy equation.

The source terms for these conservation equations are provided in Table 2 [14]. Table 3 [29,30] and Table 4 [12,14,19] show the SOEC parameters and model parameters and operating conditions.

2.3. Boundary Conditions

The anode and cathode outlet pressures are set to constant values and the mass flow rate is specified at the inlet:

$$m_a = \sum_{1}^{i} (x_i M_i) \cdot \frac{i_a A_{act} \delta_{AAL}}{4Fx_{O_2}} \cdot \xi_a \quad (39)$$

$$m_c = \sum_{1}^{i} (x_i M_i) \cdot \frac{i_c A_{act} \delta_{CAL}}{\left(2Fx_{H_2O} + 2Fx_{CO_2} + 2Fx_{CH_4}\right)} \cdot \xi_c \quad (40)$$

where A_{act} (m^2) is the active area of the cell, δ_{AAL} and δ_{CAL} (m) are the thicknesses of AAL and CAL, respectively, and ξ_a and ξ_c are the gas stoichiometry ratios of the anode and cathode.

The contact resistance between the electrode and the interconnect has a significant impact on output performance [23,40] and is particularly relevant when studying the effect of interconnect rib width. In this study, the total area-specific contact resistance (ASR) at the electrode–interconnect interface is set to 0.0132 $\Omega \cdot cm^2$ (consisting of 0.0044 $\Omega \cdot cm^2$ at the anode–interconnect interface and 0.0088 $\Omega \cdot cm^2$ at the cathode–interconnect interface) at 800 °C, as this value is representative [41]. The detailed boundary conditions and settings can be found in reference [14].

2.4. Model Validation

Four mesh systems were used to verify grid independence. The corresponding mesh numbers of the computational domain were 8800, 35,000, 88,000, and 144,000, respectively. The mesh number of 88,000 was selected for the numerical simulations. In addition, the accuracy of the model was verified by comparing the simulation results with experimental data. A SOEC with an active electrode area of 16 cm^2 was used in the experiments. It had a Ni/YSZ electrode with a thickness of 10 mm, a YSZ electrolyte with a thickness of 10 mm, and a LSM electrode with a thickness of 15 mm. Experimental data were obtained when the SOEC was at 800 °C with 45% CO_2, 45% H_2O, and 10% H_2 and pure oxygen at the cathode and anode sides, respectively. The model's structural and operational parameters were consistent with those in referenced experiments [42–44]. Figure 2 shows the experimental and simulated polarization curves. The simulation results of the polarization curves shown in the figure are in good agreement with the experimental data, indicating the reliability of the mathematical model and calculation method used in this paper.

Table 2. Source terms.

Source Terms	Unit
$S_{mass} = \begin{cases} 0 & \text{Channels} \\ S_{CH_4}+S_{H_2}+S_{CO}+S_{H_2O}+S_{CO_2} & \text{CSL, CAL} \\ S_{O_2} & \text{AAL} \end{cases}$	kg m^{-3} s^{-1}
$S_{H_2O} = \begin{cases} (-R_{MSR}-R_{WGSR})M_{H_2O} & \text{CSL} \\ -\frac{i_c}{2F}M_{H_2O} - (R_{MSR}+R_{WGSR})M_{H_2O} & \text{CAL} \end{cases}$	kg m^{-3} s^{-1}
$S_{CO_2} = \begin{cases} R_{WGSR}M_{CO_2} & \text{CSL} \\ -\frac{i_c}{2F}M_{CO_2}+R_{WGSR}M_{CO_2} & \text{CAL} \end{cases}$	kg m^{-3} s^{-1}
$S_{H_2} = \begin{cases} (3R_{MSR}+R_{WGSR})M_{H_2} & \text{CSL} \\ \frac{i_c}{2F}M_{H_2} + (3R_{MSR}+R_{WGSR})M_{H_2} & \text{CAL} \end{cases}$	kg m^{-3} s^{-1}
$S_{CO} = \begin{cases} (R_{MSR}-R_{WGSR})M_{CO} & \text{CSL} \\ \frac{i_c}{2F}M_{CO} + (R_{MSR}-R_{WGSR})M_{CO} & \text{CAL} \end{cases}$	kg m^{-3} s^{-1}
$S_{CH_4} = -R_{MSR}M_{CH_4}$ Cathode	kg m^{-3} s^{-1}
$S_{O_2} = \frac{i_a}{4F}M_{O_2}$ AAL	kg m^{-3} s^{-1}
$S_{mom} = \begin{cases} 0 & \text{Channels} \\ -\frac{\mu}{\kappa}u & \text{CAL, CSL, AAL} \end{cases}$	kg m^{-2} s^{-2}
$S_T = \begin{cases} 0 & \text{Channels} \\ \frac{{i_l}^2}{\sigma_l} & \text{Electrolyte} \\ \frac{{i_s}^2}{\sigma_s} & \text{Interconnectors} \\ \frac{{i_l}^2}{\sigma_l} + \frac{{i_s}^2}{\sigma_s}+i_a\frac{\Delta S_a T}{4F}+i_a\lvert\eta_{act}^a\rvert & \text{AAL} \\ \frac{{i_l}^2}{\sigma_l} + \frac{{i_s}^2}{\sigma_s}+i_c\frac{\Delta S_c T}{2F}+i_c\lvert\eta_{act}^c\rvert+R_{MSR}H_{MSR}+R_{WGSR}H_{WGSR} & \text{CAL} \\ \frac{{i_l}^2}{\sigma_l} + \frac{{i_s}^2}{\sigma_s}+R_{MSR}H_{MSR}+R_{WGSR}H_{WGSR} & \text{CSL} \end{cases}$	W m^{-3}
$S_{ion} = \begin{cases} -i_c & \text{CAL} \\ i_a & \text{AAL} \end{cases}$	A m^{-3}
$S_{ele} = \begin{cases} i_c & \text{CAL} \\ -i_a & \text{AAL} \end{cases}$	A m^{-3}

Table 3. Physical properties of SOEC components.

Parameters	Cathode	Anode	Electrolyte
Thermal conductivity (W m^{-1} K^{-1})	11	6	2.7
Density (kg m^{-3})	3310	3030	5160
Specific heat capacity (J kg^{-1} K^{-1})	450	430	470

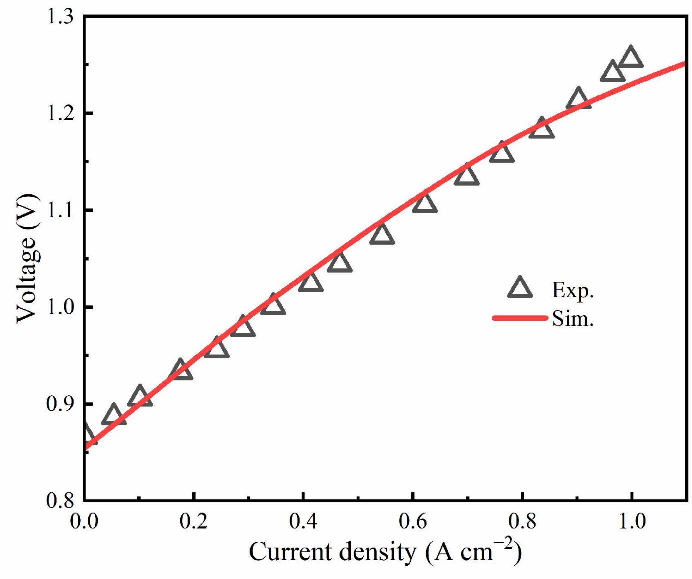

Figure 2. Comparison between the numerical results and experimental data.

Table 4. Model parameters and operating conditions.

Parameters	Value
Cathode charge transfer coefficient, α	0.65
Anode charge transfer coefficient, β	0.65
Cathode tortuosity, τ_c	3
Anode tortuosity, τ_a	3
Porosity	0.36
Exponent for exchange current density, m/n/k	0.5/0.5/0.25
Gas stoichiometry ratio, ξ_a/ξ_c	1.5/1.5
Activation energy $E_{act,c}/E_{act,a}$, J mol^{-1}	120,000/120,000
Cathode effective reaction specific surface area $S_{act,c}$, m^2 m^{-3}	2.14×10^5
Anode effective reaction specific surface area $S_{act,a}$, m^2 m^{-3}	2.14×10^5
Operating pressure (atm)	1.0
Operating temperature (K)	1073
Cathode gas composition	45 vol% H_2O, 45 vol% CO_2, 10 vol% H_2
Anode gas composition	Air (21 vol% O_2, 79 vol% N_2)

3. Results and Discussion

The influence of the rib width of the interconnect on the co-electrolysis performance of SOECs was investigated. As shown in Figure 1, the pitch width is defined as d_{pitch}, and the rib width is defined as d_{rib}. The length of the SOEC was 4 cm, the total width was 2 mm, and the d_{pitch} was fixed at 1 mm. This means that the value of d_{rib} plus half of the channel width is constant. When the d_{rib} is increased, the channel width is decreased. The flow channel and interconnector heights are kept constant. As shown in Table 5, seven different rib widths ranging from 0.2 mm to 0.8 mm with an interval of 0.1 mm were considered (CASE A, B, C, D, E, F, and G). The anode and cathode interconnectors have the same geometric parameters.

The corresponding voltages of seven cases under different current densities are presented in Figure 3a. It is observed that the voltage is increased when the current density is increased. The voltage is gradually decreased and then increased under the same current density when the d_{rib} is increased from 0.2 mm to 0.8 mm, especially at high current densities. The voltages of seven cases at the current density of 1 A/cm^2 are summarized in Figure 3b. The voltages of CASE A, CASE E, and CASE G are 1.272 V, 1.213 V, and 1.221 V, respectively. These results demonstrate that cell performance is greatly affected by the rib width, and the best performance can be achieved by CASE E, which has a rib width of 0.6 mm. The variation in voltage is caused by the equilibrium potential and overpotentials. As the rib width increases, the interface area between the interconnector and the electrode increases, the contact resistance decreases, and the ohmic overpotential decreases. This phenomenon is more pronounced at high current densities. When the rib width is increased, the area of the flow channel decreases, which hinders the diffusion and transmission of gas, leading to a reduction in the concentration of reaction gas at the active sites in the active layers.

Table 5. Dimensions of interconnect ribs of SOEC.

	d_{rib} (mm)	d_{pitch} (mm)
CASE A	0.2	1
CASE B	0.3	1
CASE C	0.4	1
CASE D	0.5	1
CASE E	0.6	1
CASE F	0.7	1
CASE G	0.8	1

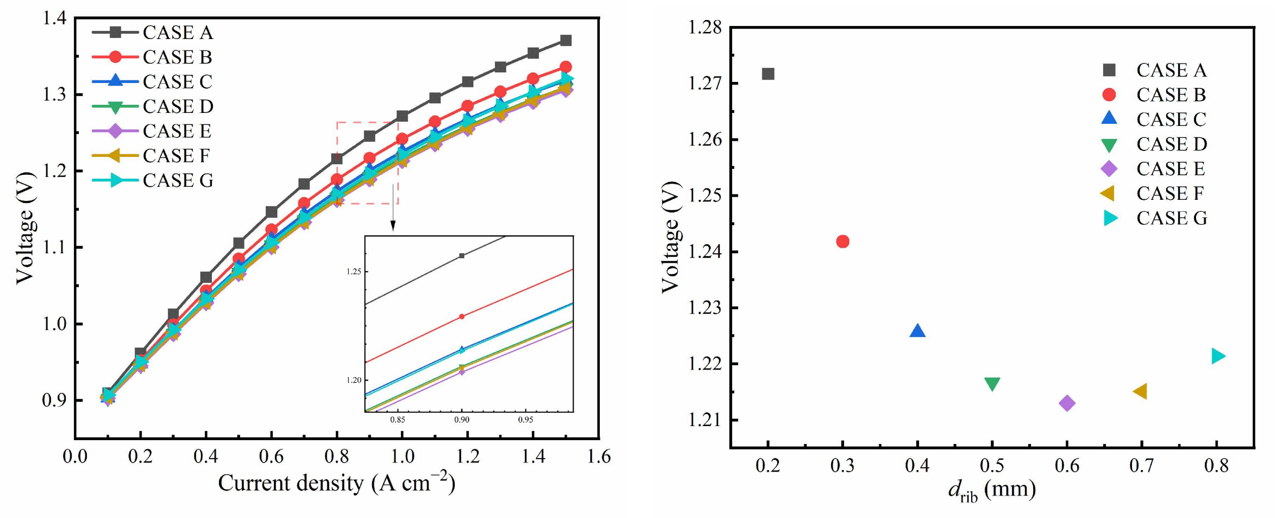

(**a**) (**b**)

Figure 3. (**a**) Polarization curves of SOECs; (**b**) the corresponding voltages of SOECs under the current density of 1 A/cm^2.

Figure 4 shows the mole fraction distributions of H_2O, CO_2, H_2, CO, and CH_4 in the cathode side of SOECs. In this figure, the *x*-axis is the direction of gas flow, the *y*-axis is the direction of cell width, and the *z*-axis is the direction of cell thickness. As shown in Figure 4a,b, the mole fractions of H_2O and CO_2 are gradually decreased along the channel direction. H_2O and CO_2 are consumed in the cathode active layer caused by the electrochemical reactions. The mole fractions in the porous electrode are gradually decreased as the rib width is increased. The minimum mole fractions of H_2O and CO_2 obtained by CASE G are 0.211 and 0.254, respectively. This is because the increase in rib width hinders the transport processes of H_2O and CO_2 from the flow channel to the active layer. As can be seen from Figure 4c,d, the mole fractions of H_2 and CO are gradually increased along the flow direction, and the mole fractions of them in the support layer and active layer are higher than those in the flow channel. The mole fractions of H_2 and CO increase with the increase in rib width, and the maximum mole fractions of them in CASE

G are 0.276 and 0.259, respectively. It can be seen from Figure 4e that CH_4 mole fractions in the active layer and support layer are gradually increased along the flow direction and are very low in the flow channel. The maximum mole fraction of CH_4 is increased from 9.33×10^{-6} to 1.31×10^{-4} when the rib width is increased. These findings indicate that the reverse MSR reaction rate is very low.

Figure 5 shows the reaction rates of WGSR and MSR of SOECs with different rib widths. The negative sign in the figure represents the reverse direction of reactions. As shown in Figure 5a, the reverse WGSR rate is decreased when the rib width is increased. When the current density is 1 A cm^{-2}, the reverse WGSR rates of CASE A and CASE G are 49.82 mol m^{-3} s^{-1} and 22.52 mol m^{-3} s^{-1}, respectively. As shown in Figure 5b, the reverse MSR reaction rate is increased with the increase in current density. Meanwhile, it is increased with the increase in rib width. When the current density is 1 A cm^{-2}, the reverse MSR rates of CASE A and CASE G are 0.0041 mol m^{-3} s^{-1} and 0.0208 mol m^{-3} s^{-1}, respectively. This is because that mole fraction of H_2O is decreased and mole fractions of H_2 and CO are increased as discussed above. Figure 6 shows the WGSR and MSR rate distributions in the porous electrode. In this figure, the x-axis is the direction of gas flow, the y-axis is the direction of cell width, and the z-axis is the direction of cell thickness. The reverse WGSR rate under the channel region is higher than that under the rib region, and the maximum reverse WGSR rate is observed at the entrance of the channel region. The maximum and minimum reverse WGSR rates of seven cases are 226.61 mol m^{-3} s^{-1} and 2.24 mol m^{-3} s^{-1}, respectively. The reverse MSR rate under the channel region is lower than that under the rib region. The reverse MSR rate under the rib region is gradually increased when the rib width is increased.

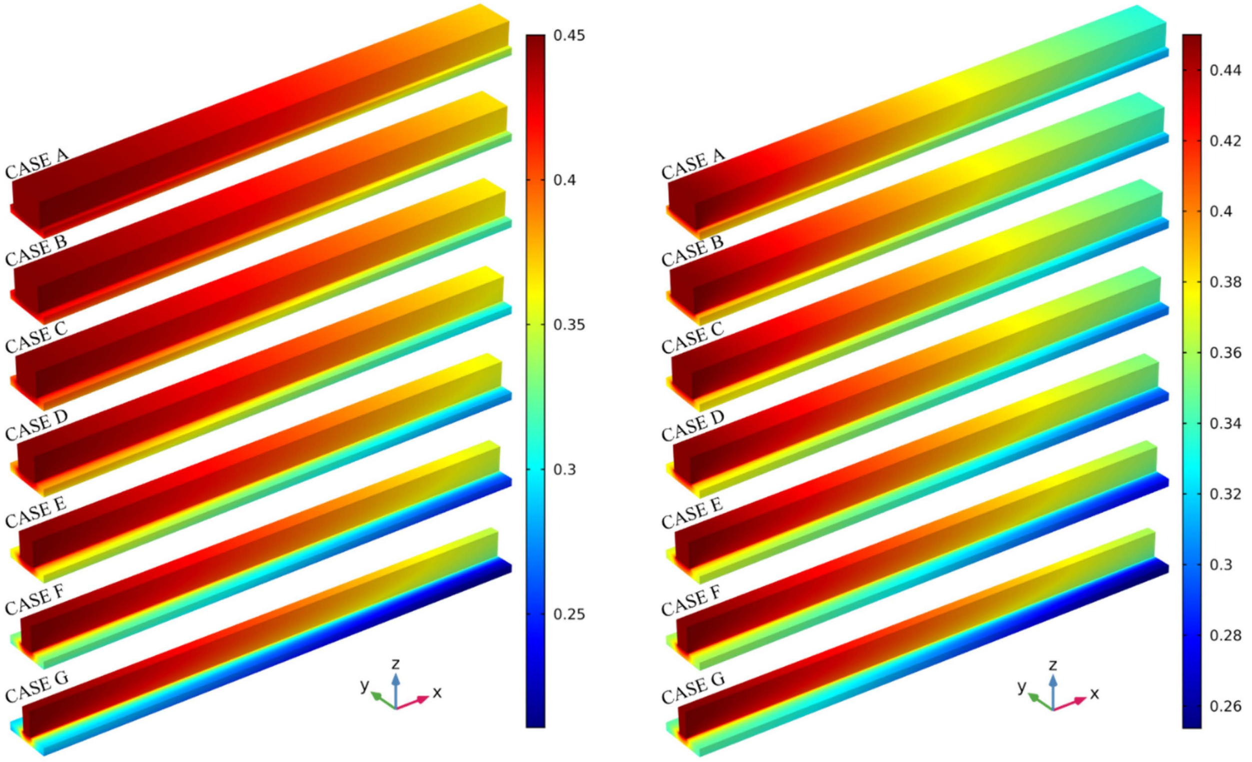

(a) **(b)**

Figure 4. *Cont.*

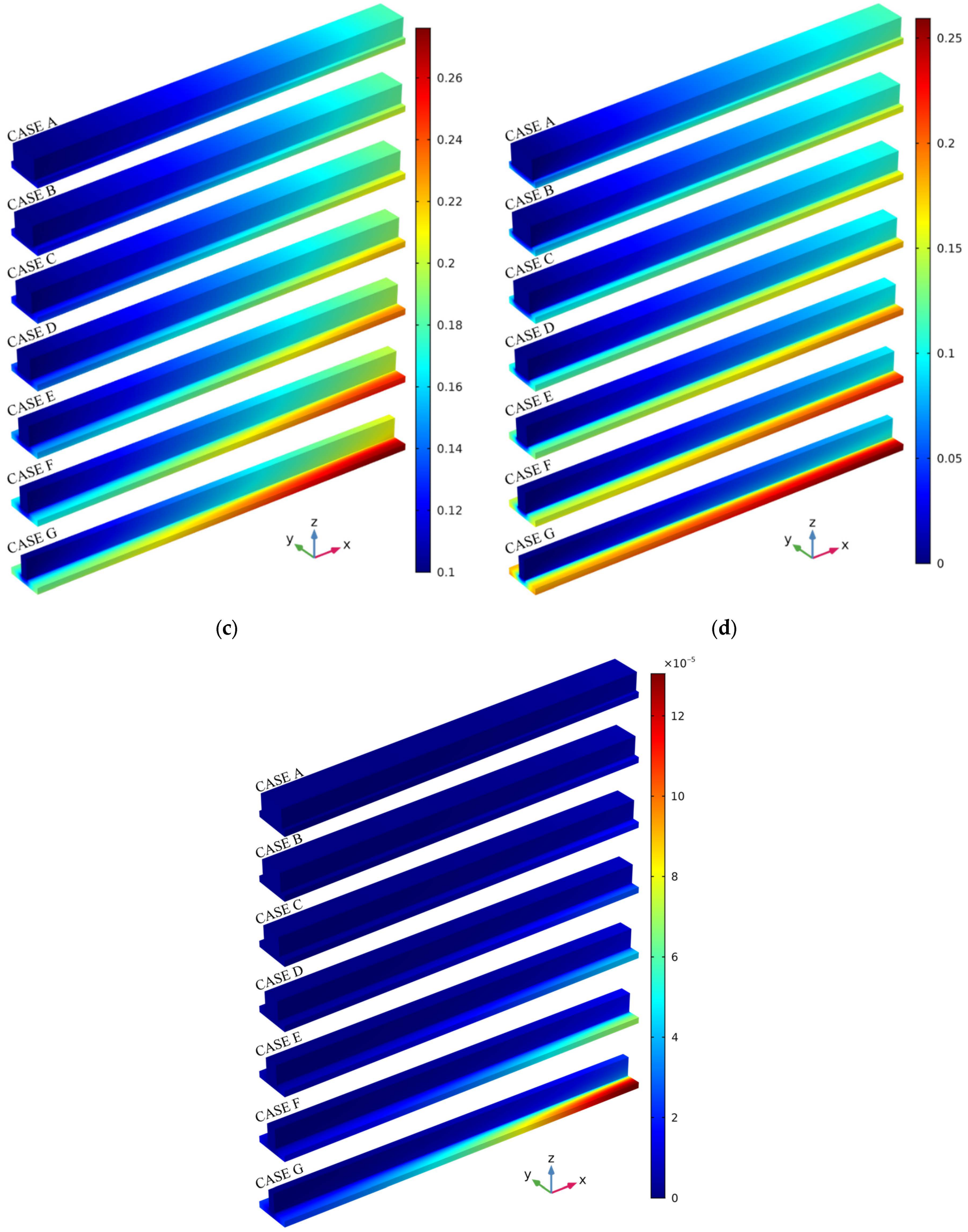

(**c**) (**d**)

(**e**)

Figure 4. The mole fraction distributions: (**a**) H_2O; (**b**) CO_2; (**c**) H_2; (**d**) CO; (**e**) CH_4.

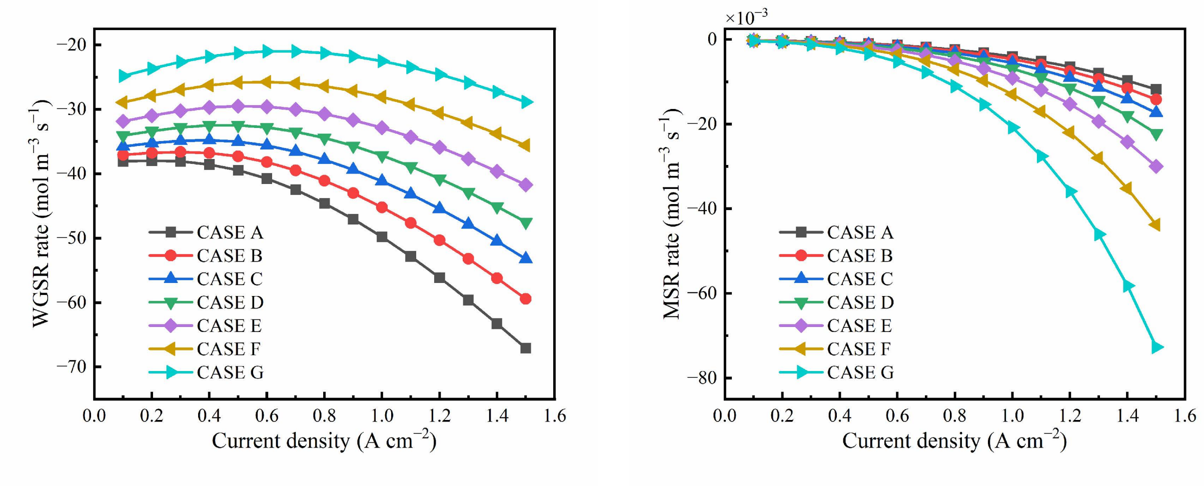

(**a**) (**b**)

Figure 5. The reaction rates of SOECs: (**a**) the WGSR rate; (**b**) the MSR rate.

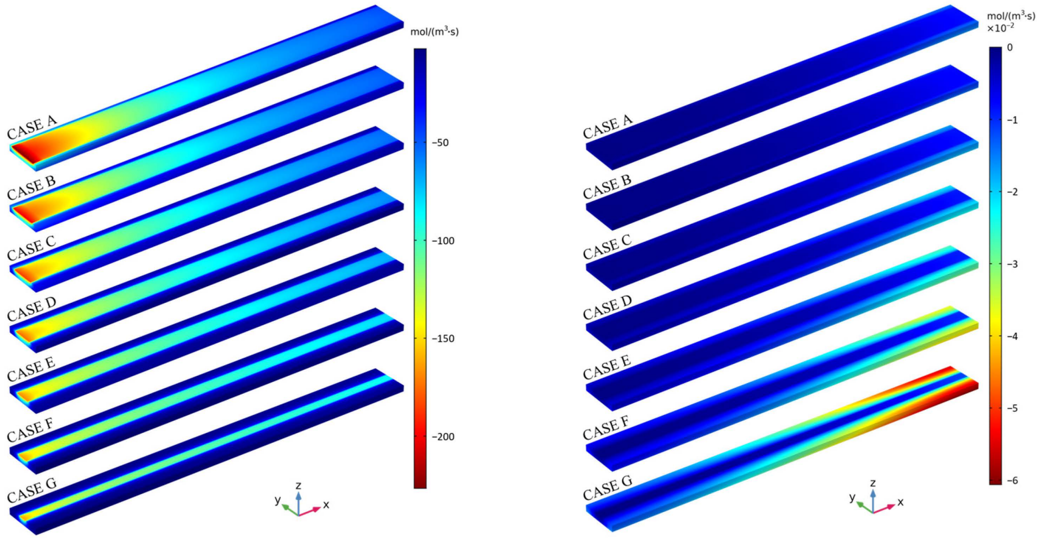

(**a**) (**b**)

Figure 6. The distributions of reaction rates in SOECs: (**a**) the WGSR rate; (**b**) the MSR rate.

The velocity distributions in the cathode flow channel and electrode of SOECs with different rib widths are presented in Figure 7. In this figure, the *x*-axis is the direction of gas flow, the *y*-axis is the direction of cell width, and the *z*-axis is the direction of cell thickness. The velocity in the electrode is very small, and the gas transport is mainly dominated by the diffusion process. The maximum velocity is observed in the flow channel center, and it is also increased from CASE A to CASE G. This is because the rib width is increased and then the flow channel area is decreased. A constant mass flow rate is specified at the inlet of the flow channel, and the velocity is accordingly increased. The cathode flow channel pressure drops of the SOECs are shown in Figure 8. It is clearly observed that the pressure drop is increased from CASE A to CASE G. The pressure drops of seven cases are 18.52 Pa, 22.83 Pa, 29.77 Pa, 42.11 Pa, 66.92 Pa, 130.31 Pa, and 368.52 Pa, respectively.

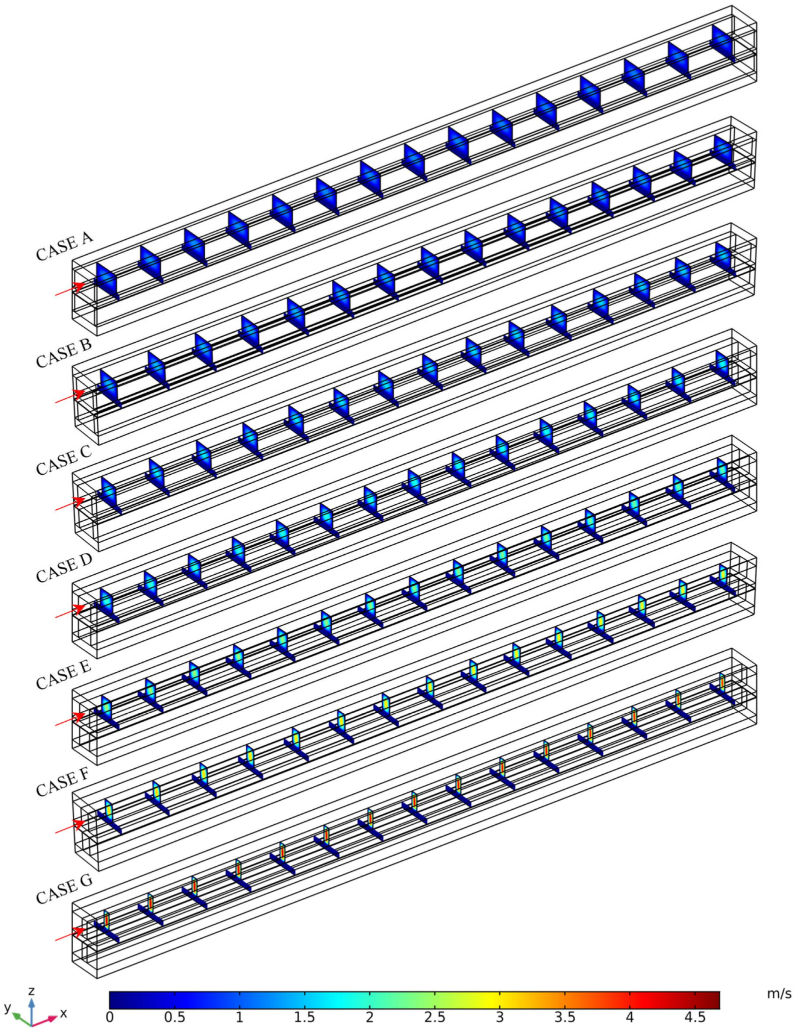

Figure 7. The cathode side velocity distributions of SOECs.

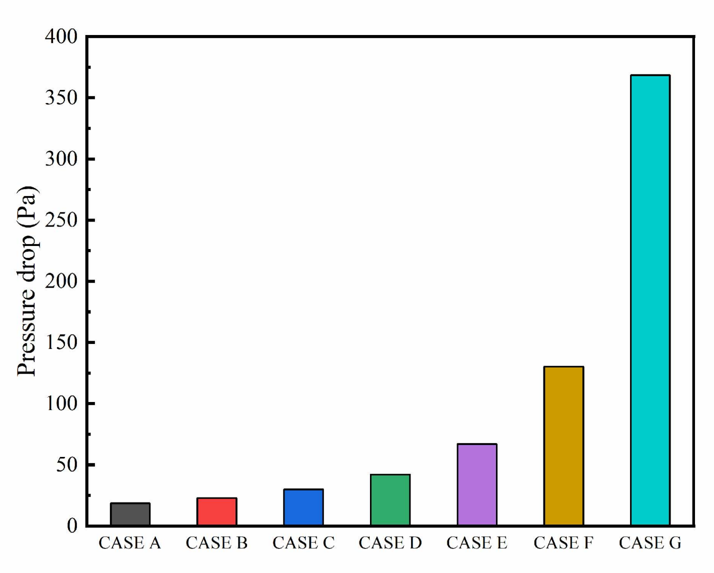

Figure 8. The cathode flow channel pressure drops of SOECs.

The temperature distributions at the middle plane of SOECs with different rib widths are presented in Figure 9. The temperature is gradually decreased along the flow direction.

The maximum temperature appears at the flow channel region. The maximum temperature that appears is 1073 K, and the minimum temperatures of the seven cases are 1053.46 K, 1041.82 K, 1034.98 K, 1030.63 K, 1027.91 K, 1026.39 K, and 1025.82 K, respectively. The corresponding temperature differences of the seven cases are 19.54 K, 31.18 K, 38.02 K, 42.37 K, 45.09 K, 46.61 K, and 47.18 K, respectively. These indicate that the SOECs are under the endothermic process and the temperature of the SOEC decreases as the rib width increases.

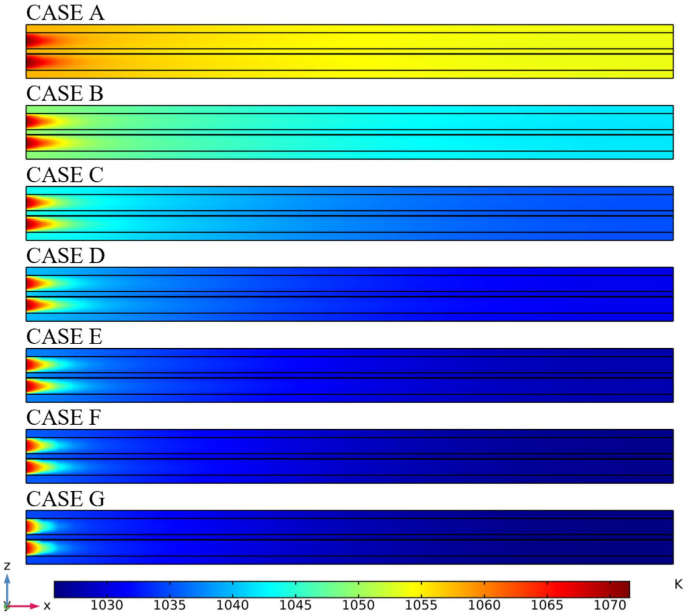

Figure 9. The middle plane temperature distributions of SOECs.

4. Conclusions

A three-dimensional model for the co-electrolysis of water and carbon dioxide in SOECs was developed to examine the effect of interconnector rib width on performance and transport phenomena. The mathematical model was verified by comparing the numerical results with experimental data. The gas transport, heat transfer, mass transfer, ion transport, electron transport, electrochemical, and chemical reaction processes within the cell were considered in detail. The following conclusions were obtained.

The voltage of SOEC is decreased and then increases as the rib width is increased from 0.2 mm to 0.8 mm. The optimal performance is obtained from the SOEC with a rib width of 0.6 mm. The reverse WGSR rate is decreased, and the reverse MSR rate is increased with increasing rib width. When the rib width is increased, the flow channel area is decreased, and the velocity is increased. Accordingly, the pressure drop of the flow channel is also increased. In addition, the distributions of species mole fractions and temperature are affected by the rib width. These indicate that the cell performance of SOECs can be improved by optimizing the structure of interconnectors. The obtained results can improve the understanding of transport phenomena in SOECs with different rib widths and provide guidelines for the design of interconnectors of SOECs.

Author Contributions: Conceptualization, S.L. and Z.Y.; methodology, S.L.; software, Z.Y.; validation, Z.Y. and S.L.; formal analysis, Z.Y.; investigation, S.L.; writing—original draft preparation, S.L. and Z.Y.; writing—review and editing, Q.S. and G.Y.; supervision, Q.S.; project administration, S.L.; funding acquisition, S.L. All authors have read and agreed to the published version of the manuscript.

Funding: This research was funded by the National Natural Science Foundation of China, grant number 52001045, and the Science and Technology Innovation Foundation of Dalian, grant number 2021JJ11CG004.

Institutional Review Board Statement: Not applicable.

Informed Consent Statement: Not applicable.

Data Availability Statement: Not applicable.

Conflicts of Interest: The authors declare no conflict of interest.

References

1. Zhao, Z.; Wang, Z.; Xie, S.; Zhang, M.; Ouyang, T. A novel design of power-cooling cogeneration system driven by solid oxide fuel cell waste heat in ocean-going vessels. *J. Clean. Prod.* **2021**, *318*, 128532. [CrossRef]
2. Guan, W.; Chen, J.; Chen, L.; Cao, J.; Fan, H. Safe Design of a Hydrogen-Powered Ship: CFD Simulation on Hydrogen Leakage in the Fuel Cell Room. *J. Mar. Sci. Eng.* **2023**, *11*, 651. [CrossRef]
3. Cavo, M.; Gadducci, E.; Rattazzi, D.; Rivarolo, M.; Magistri, L. Dynamic analysis of PEM fuel cells and metal hydrides on a zero-emission ship: A model-based approach. *Int. J. Hydrogen Energy* **2021**, *46*, 32630–32644. [CrossRef]
4. Ababneh, H.; Hameed, B.H. Electrofuels as emerging new green alternative fuel: A review of recent literature. *Energy Convers. Manag.* **2022**, *254*, 115213. [CrossRef]
5. Wang, X.; Zhu, J.; Han, M. Industrial Development Status and Prospects of the Marine Fuel Cell: A Review. *J. Mar. Sci. Eng.* **2023**, *11*, 238. [CrossRef]
6. Shim, H.; Kim, Y.H.; Hong, J.; Hwang, D.; Kang, H.J. Marine Demonstration of Alternative Fuels on the Basis of Propulsion Load Sharing for Sustainable Ship Design. *J. Mar. Sci. Eng.* **2023**, *11*, 567. [CrossRef]
7. Osman, A.I.; Mehta, N.; Elgarahy, A.M.; Hefny, M.; Al-Hinai, A.; Al-Muhtaseb, A.H.; Rooney, D.W. Hydrogen production, storage, utilisation and environmental impacts: A review. *Environ. Chem. Lett.* **2022**, *20*, 153–188. [CrossRef]
8. Rezk, H.; Olabi, A.G.; Abdelkareem, M.A.; Alahmer, A.; Sayed, E.T. Maximizing Green Hydrogen Production from Water Electrocatalysis: Modeling and Optimization. *J. Mar. Sci. Eng.* **2023**, *11*, 617. [CrossRef]
9. Hu, K.; Fang, J.; Ai, X.; Huang, D.; Zhong, Z.; Yang, X.; Wang, L. Comparative study of alkaline water electrolysis, proton exchange membrane water electrolysis and solid oxide electrolysis through multiphysics modeling. *Appl. Energy* **2022**, *312*, 118788. [CrossRef]
10. Ni, M. An electrochemical model for syngas production by co-electrolysis of H_2O and CO_2. *J. Power Sources* **2012**, *202*, 209–216. [CrossRef]
11. Ni, M. 2D thermal modeling of a solid oxide electrolyzer cell (SOEC) for syngas production by H_2O/CO_2 co-electrolysis. *Int. J. Hydrogen Energy* **2012**, *37*, 6389–6399. [CrossRef]
12. Luo, Y.; Shi, Y.; Li, W.; Cai, N. Comprehensive modeling of tubular solid oxide electrolysis cell for co-electrolysis of steam and carbon dioxide. *Energy* **2014**, *70*, 420–434. [CrossRef]
13. Xie, Y.; Xue, X. Modeling of solid oxide electrolysis cell for syngas generation with detailed surface chemistry. *Solid State Ion* **2012**, *224*, 64–73. [CrossRef]
14. Du, Y.; Qin, Y.; Zhang, G.; Yin, Y.; Jiao, K.; Du, Q. Modelling of effect of pressure on co-electrolysis of water and carbon dioxide in solid oxide electrolysis cell. *Int. J. Hydrogen Energy* **2019**, *44*, 3456–3469. [CrossRef]
15. Kazempoor, P.; Braun, R.J. Model validation and performance analysis of regenerative solid oxide cells: Electrolytic operation. *Int. J. Hydrogen Energy* **2014**, *39*, 2669–2684. [CrossRef]
16. Ni, M.; LEUNG, M.; LEUNG, D. Parametric study of solid oxide steam electrolyzer for hydrogen production. *Int. J. Hydrogen Energy* **2007**, *32*, 2305–2313. [CrossRef]
17. Menon, V.; Fu, Q.; Janardhanan, V.M.; Deutschmann, O. A model-based understanding of solid-oxide electrolysis cells (SOECs) for syngas production by H_2O/CO_2 co-electrolysis. *J. Power Sources* **2015**, *274*, 768–781. [CrossRef]
18. Li, W.; Shi, Y.; Luo, Y.; Cai, N. Elementary reaction modeling of CO_2/H_2O co-electrolysis cell considering effects of cathode thickness. *J. Power Sources* **2013**, *243*, 118–130. [CrossRef]
19. Wang, Y.; Du, Y.; Ni, M.; Zhan, R.; Du, Q.; Jiao, K. Three-dimensional modeling of flow field optimization for co-electrolysis solid oxide electrolysis cell. *Appl. Therm. Eng.* **2020**, *172*, 114959. [CrossRef]
20. Zhao, J.; Lin, Z.; Zhou, M. Three-Dimensional Modeling and Performance Study of High Temperature Solid Oxide Electrolysis Cell with Metal Foam. *Sustainability* **2022**, *14*, 7064. [CrossRef]
21. Lin, Z.; Stevenson, J.W.; Khaleel, M.A. The effect of interconnect rib size on the fuel cell concentration polarization in planar SOFCs. *J. Power Sources* **2003**, *117*, 92–97. [CrossRef]
22. Jeon, D.H.; Nam, J.H.; Kim, C. Microstructural Optimization of Anode-Supported Solid Oxide Fuel Cells by a Comprehensive Microscale Model. *J. Electrochem. Soc.* **2006**, *153*, A406–A417. [CrossRef]
23. Kong, W.; Li, J.; Liu, S.; Lin, Z. The influence of interconnect ribs on the performance of planar solid oxide fuel cell and formulae for optimal rib sizes. *J. Power Sources* **2012**, *204*, 106–115. [CrossRef]
24. Liu, S.; Kong, W.; Lin, Z. Three-dimensional modeling of planar solid oxide fuel cells and the rib design optimization. *J. Power Sources* **2009**, *194*, 854–863. [CrossRef]
25. Costamagna, P.; Honegger, K. Modeling of solid oxide heat exchanger integrated stacks and simulation at high fuel utilization. *J. Electrochem. Soc.* **1998**, *145*, 3995–4007. [CrossRef]

26. Park, J.; Bae, J. Characterization of electrochemical reaction and thermo-fluid flow in metal-supported solid oxide fuel cell stacks with various manifold designs. *Int. J. Hydrogen Energy* **2012**, *37*, 1717–1730. [CrossRef]
27. Li, W.; Wang, H.; Shi, Y.; Cai, N. Performance and methane production characteristics of H_2O-CO_2 co-electrolysis in solid oxide electrolysis cells. *Int. J. Hydrogen Energy* **2013**, *38*, 11104–11109. [CrossRef]
28. Khazaee, I.; Rava, A. Numerical simulation of the performance of solid oxide fuel cell with different flow channel geometries. *Energy* **2017**, *119*, 235–244. [CrossRef]
29. Lin, B.; Shi, Y.; Cai, N. Numerical simulation of cell-to-cell performance variation within a syngas-fuelled planar solid oxide fuel cell stack. *Appl. Therm. Eng.* **2017**, *114*, 653–662. [CrossRef]
30. Andersson, M.; Yuan, J.; Sundén, B. SOFC modeling considering hydrogen and carbon monoxide as electrochemical reactants. *J. Power Sources* **2013**, *232*, 42–54. [CrossRef]
31. Sun, Y.; Zheng, W.; Ji, S.; Sun, A.; Shuai, W.; Zheng, N.; Han, Y.; Xiao, G.; Ni, M.; Xu, H. Dynamic behavior of high-temperature CO_2/H_2O co-electrolysis coupled with real fluctuating renewable power. *Sustain. Energy Technol. Assess.* **2022**, *52*, 102344. [CrossRef]
32. Ni, M. Modeling and parametric simulations of solid oxide fuel cells with methane carbon dioxide reforming. *Energy Convers. Manag.* **2013**, *70*, 116–129. [CrossRef]
33. Haberman, B.A.; Young, J.B. Three-dimensional simulation of chemically reacting gas flows in the porous support structure of an integrated-planar solid oxide fuel cell. *Int. J. Heat Mass Transf.* **2004**, *47*, 3617–3629. [CrossRef]
34. Chen, Y.; Luo, Y.; Shi, Y.; Cai, N. Theoretical modeling of a pressurized tubular reversible solid oxide cell for methane production by co-electrolysis. *Appl. Energy* **2020**, *268*, 114927. [CrossRef]
35. Suwanwarangkul, R.; Croiset, E.; Fowler, M.W.; Douglas, P.L.; Entchev, E.; Douglas, M.A. Performance comparison of Fick's, dusty-gas and Stefan-Maxwell models to predict the concentration overpotential of a SOFC anode. *J. Power Sources* **2003**, *122*, 9–18. [CrossRef]
36. Li, S.; Yang, Z.; Liu, Y.; Shen, Q.; Yang, G.; Sunden, B.A. Analysis of heat and mass transport characteristics in microchannel reactors with non-uniform catalyst distributions for hydrogen production. *Int. J. Numer. Methods Heat Fluid Flow* **2022**, *32*, 3191–3209. [CrossRef]
37. Yakabe, H.; Hishinuma, M.; Uratani, M.; Matsuzaki, Y.; Yasuda, I. Evaluation and modeling of performance of anode-supported solid oxide fuel cell. *J. Power Sources* **2000**, *86*, 423–431. [CrossRef]
38. Li, W.; Shi, Y.; Luo, Y.; Cai, N. Elementary reaction modeling of solid oxide electrolysis cells: Main zones for heterogeneous chemical/electrochemical reactions. *J. Power Sources* **2015**, *273*, 1–13. [CrossRef]
39. Todd, B.; Young, J.B. Thermodynamic and transport properties of gases for use in solid oxide fuel cell modelling. *J. Power Sources* **2002**, *110*, 186–200. [CrossRef]
40. Kornely, M.; Leonide, A.; Weber, A.; Ivers-Tiffée, E. Performance limiting factors in anode-supported cells originating from metallic interconnector design. *J. Power Sources* **2011**, *196*, 7209–7216. [CrossRef]
41. Fu, Q.; Li, Z.; Wei, W.; Liu, F.; Xu, X.; Liu, Z. Performance enhancement of a beam and slot interconnector for anode-supported SOFC stack. *Energy Convers. Manag.* **2021**, *241*, 114277. [CrossRef]
42. Ebbesen, S.D.; Graves, C.; Mogensen, M. Production of Synthetic Fuels by Co-Electrolysis of Steam and Carbon Dioxide. *Int. J. Green Energy* **2009**, *6*, 646–660. [CrossRef]
43. Ebbesen, S.D.; Knibbe, R.; Mogensen, M. Co-Electrolysis of Steam and Carbon Dioxide in Solid Oxide Cells. *J. Electrochem. Soc.* **2012**, *159*, F482–F489. [CrossRef]
44. Graves, C.; Ebbesen, S.D.; Mogensen, M. Co-electrolysis of CO_2 and H_2O in solid oxide cells: Performance and durability. *Solid State Ion* **2011**, *192*, 398–403. [CrossRef]